Monthly Notices of the ROYAL ASTRONOMICAL SOCIETY

MNRAS **499,** 2138–2147 (2020) doi:10.1093/mnras/staa2823
Advance Access publication 2020 September 18

The ULX source X-3 in NGC 4258: a search for its X-ray and optical properties

A. Akyuz [1,2★] S. Avdan [2] S. Allak [2,3] N. Aksaker [2,4] I. Akkaya Oralhan [5] and S. Balman [6,7]

[1]*Department of Physics, University of Çukurova, 01330 Adana, Turkey*
[2]*Space Science and Solar Energy Research and Application Center (UZAYMER), University of Çukurova, 01330 Adana, Turkey*
[3]*Department of Physics, University of Çanakkale Onsekiz Mart, 17020 Çanakkale, Turkey*
[4]*Adana Organised Industrial Zones Vocational School of Technical Science, University of Çukurova, 01410 Adana, Turkey*
[5]*Department of Astronomy and Space Sciences, Erciyes University, 38039 Kayseri, Turkey*
[6]*Department of Astronomy and Space Sciences, Istanbul University, 34119 Istanbul, Turkey*
[7]*Faculty of Engineering and Natural Sciences, Kadir Has University, Cibali, 34083 Istanbul, Turkey*

Accepted 2020 September 14. Received 2020 August 12; in original form 2020 March 22

ABSTRACT

We present the results of a search for the nature of ultraluminous X-ray source (ULX) X-3 in the nearby galaxy NGC 4258. We use archival data from *XMM–Newton*, *Chandra*, *NuSTAR*, and *Hubble Space Telescope* (*HST*) observations. Total X-ray data were analysed to find that the model parameters of the system are indicative of a stellar-mass black hole, $\sim$10 $M_{\odot}$, as the central compact object. Furthermore, analyses of the optical data from *HST* reveal two optical candidates at 90 per cent confidence level within an error radius of 0.28 arcsec. Assuming the optical emission is dominated by the donor star, both of these candidates are found to have spectral types that lie between B3 and F1 with absolute magnitudes of $M_V \approx -6.4$. Moreover, the age and mass estimates for the candidates are found to be 10 and 18 Myr and 13 and 20 $M_{\odot}$, respectively.

Key words: galaxies: individual: NGC 4258 – X-rays: binaries.

1 INTRODUCTION

Ultraluminous X-ray sources (ULXs) are off-nuclear point sources in a number of external galaxies. The X-ray luminosity of such a source is usually $L_X \sim 10^{39}$ erg s^{-1}, exceeding the Eddington limit for a typical 10-$M_{\odot}$ stellar-remnant black hole (see the review by Kaaret, Feng & Roberts 2017). Models of ULXs proposed to explain the high luminosities of ULXs require that a central accretor in the form of a black hole should exist as a driving engine. This proposed picture represents sources that may be either stellar or intermediate-mass black holes. If a ULX hosts a stellar-mass black hole (sMBH), the high luminosity is generated by super-Eddington accretion on to the stellar-mass accretor (Poutanen et al. 2013; Sutton, Roberts & Middleton 2013; Motch et al. 2014; Fabrika et al. 2015). However, if a ULX hosts an intermediate-mass black hole (IMBH), the high luminosity could then be explained by sub-Eddington accretion on to such sources (Miller & Colbert 2004; Farrell et al. 2009; Mezcua et al. 2015).

However, recent discoveries proved that some ULXs do show coherent pulsations and they are classified as pulsating ULXs (PULXs). In this case, the luminosity is generated from super-Eddington accretion on to a magnetized neutron star orbiting a stellar companion (Bachetti et al. 2014; Fürst et al. 2016; Israel et al. 2017a, b; Carpano et al. 2018; Rodríguez Castillo et al. 2020; Sathyaprakash et al. 2019). Hence the debate about the type of dominant ULX accretor continues (King & Lasota 2016; Wiktorowicz et al. 2017).

Based on high-quality *XMM–Newton* and *Chandra* data, it became clear that the observed X-ray spectra of ULXs are different from those of Galactic black hole binaries (BHBs). The majority of ULX spectra revealed a curvature that is described by a cut-off usually at $\sim$3–7 keV, and mostly accompanied by a soft excess. The curvature is often interpreted either as an effect of a cold optically thick corona or emission from the inner regions of a geometrically thick accretion disc (Stobbart, Roberts & Wilms 2006; Roberts 2007; Gladstone, Roberts & Done 2009). These spectral features suggest a new *ultra-luminous* accretion state for ULXs, where super-Eddington accretion flows on to a black hole or, as recent pulsating ULXs show, on to a neutron star occur. Broad-band *NuSTAR* observations have clarified that the curvature of ULX spectra has a high-energy cut-off extending above 10 keV. On the other hand, for Galactic BHBs, this spectral cut-off typically exceeds $\sim$60 keV (Bachetti et al. 2013; Luangtip, Roberts & Done 2016; Fürst et al. 2017; Pintore et al. 2017).

Optical studies of ULXs also have important implications for understanding the nature of these sources and their environments. In particular, the optical identification of counterparts may give us valuable information on the mass and spectral type of the companion star and the origin of the optical emission. This emission is thought to originate from the accretion disc by reprocessing of X-rays in the outer disc regions and/or from the companion star. So far, single or multiple optical counterparts have been identified for about 30 ULXs using ground-based telescopes and the *Hubble Space Telescope* (*HST*) (Soria et al. 2005; Tao et al. 2011; Grisé et al. 2011, 2012; Gladstone et al. 2013; Avdan et al. 2016a, 2019; Aksaker et al. 2019).

Spectra of optical counterparts usually allow us to construct radial velocity curves. However, optical spectra of ULXs generally lack

★ E-mail: aakyuz@cu.edu.tr

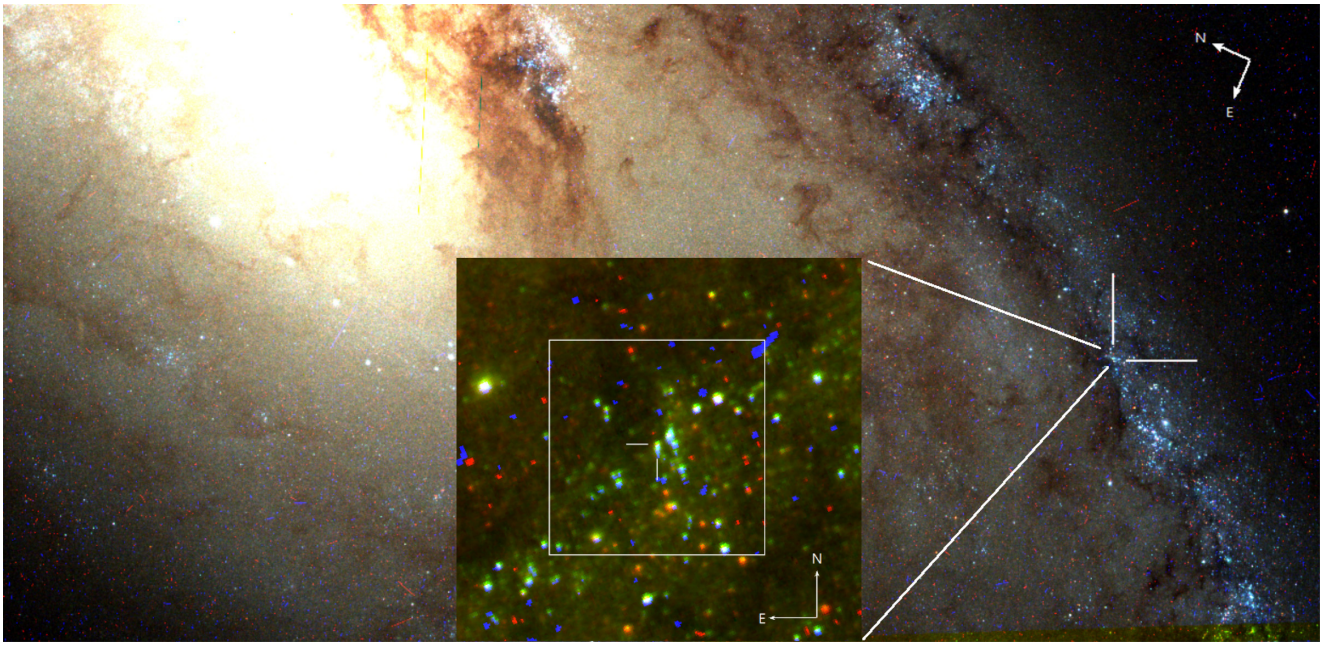

Figure 1. The *HST*/ACS true colour image of galaxy NGC 4258. Red, green, and blue colours represent F814W, F555W, and F435W filters, respectively. The X-3 position is marked with white bars. In the zoomed image, the 5 × 5 arcsec^2 white box contains X-3 and field stars.

traceable absorption lines (most likely due to their faintness ($m_V \geq 21$)), or have high-energy emission lines like He II λ4686 that do not seem to trace any clear orbital movement. Even in the case of P13, where absorption lines from the companion star are visible, they do not trace any orbital movement in the system. They are most likely due to X-ray (uneven) heating of the donor star (Motch et al. 2014).

The absolute magnitudes and colour indices of optical counterparts are found to lie in the intervals $M_V = -3$ to -8 and $B - V = -6$ to $+0.4$, respectively. ULX systems most probably contain OB supergiant donors. The blue colour observed is thought to arise from X-ray reprocessing in the accretion disc or the donor star, or both (Patruno & Zampieri 2010; Jonker et al. 2012; Vinokurov, Fabrika & Atapin 2018). However, some ULXs do contain red supergiant companions in the near-infrared band (Heida et al. 2014, 2016; López et al. 2017).

Most ULXs are found to be located inside star-forming regions and a few of them are reported to be powering the surrounding nebula by their radiation and/or outflows (Pakull & Mirioni 2003; Abolmasov et al. 2007; Kaaret et al. 2017). There are also many ULXs associated with young (5–20 Myr) star clusters, helping us to understand some of their subtle properties (Soria et al. 2005; Grisé et al. 2011; Poutanen et al. 2013; Avdan et al. 2016a, b).

In the present study, we searched for the X-ray spectral and temporal properties and also optical counterpart(s) of ULX X-3 (hereafter X-3) in NGC 4258 using archival *XMM–Newton*, *Chandra*, *NuSTAR*, and *HST* observations. This source is identified as a ULX with an X-ray luminosity of $L_X = 5.3 \times 10^{39}$ erg s^{-1} by Swartz et al. (2011). NGC 4258 is classified as a Seyfert-type spiral galaxy at a distance of 7.7 Mpc (de Vaucouleurs et al. 1991). Our target source in NGC 4258 appears as a bright point-like source in the X-ray images. The source is located to the south of an arm at RA = $12^h18^m57\overset{s}{.}8$, Dec. = $+47^\circ16'07''$ and 2.1 arcmin away from the galaxy centre. The true-colour *HST* image of NGC 4258 is given in Fig. 1 and the ULX is marked by lines.

The present introduction will be followed by a description of observations and details of the data analysis in Section 2. Discussion and conclusions regarding the X-ray spectral analysis and optical properties of X-3 are presented in Section 3.

Table 1. The log of *XMM–Newton*, *Chandra*, and *NuSTAR* observations.

	Label	ObsID	Date	Exp. (ks)
XMM–Newton	XM1	0110920101	2000-12-08	23.31
	XM2	0059140101	2001-05-06	12.70
	XM3	0059140201	2001-06-17	13.16
	XM4	0059140401	2001-12-17	15.01
	XM5	0059140901	2002-05-23	16.51
	XM6	0203270201	2004-06-01	48.91
	XM7	0400560301	2006-11-18	64.52
Chandra	Ch1	700234	2001-05-28	20.94
NuSTAR	N1	60101046002	2015-11-16	54.78
	N2	60101046004	2016-01-10	103.6

2 OBSERVATIONS AND ANALYSIS RESULTS

2.1 X-ray observations

The source X-3 was observed by the *XMM–Newton*, *Chandra*, and *NuSTAR* satellites several times. The observations used in this study are listed in Table 1.

The *XMM–Newton* data were analysed with the standard Science Analysis Software (SAS, v16.0.0) with well-defined analysis steps. Events corresponding to single–double pixels (PATTERN ≤12) and single–multiple (PATTERN ≤4) with FLAG = 0 were selected for EPIC MOS and PN cameras, respectively. The source and background spectra were extracted using 15-arcsec circular regions with the *evselect* task in SAS. Only XM7 data were affected by the background flaring. The last 3 ks of data were removed from the observation prior to source and background extraction. The average

Table 2. Best-fitting spectral parameters for X-3 from the *XMM–Newton* and *Chandra* observations. The errors are 90 per cent for each parameter.

No.	$N_{\rm H}$	Γ^a	Γ^*	$kT_{\rm in}{}^b$	$kT_{\rm in}{}^*$	χ^2_ν (dof)^c	χ^{2*}_ν (dof)	$L_{\rm X}{}^d$	$L_{\rm X}{}^*$
–	(10^{22} cm^{-2})	–		(keV)	(keV)	–		(10^{39} erg s^{-1})	(10^{39} erg s^{-1})
				tbabs × pl					
XM1	$0.39^{+0.04}_{-0.04}$	$2.15^{+0.14}_{-0.14}$	$2.43^{+0.16}_{-0.16}$	–	–	1.24 (35)	1.29 (38)	$1.83^{+0.17}_{-0.17}$	$2.31^{+0.17}_{-0.17}$
XM2	$0.55^{+0.07}_{-0.06}$	$2.27^{+0.15}_{-0.15}$	$2.23^{+0.16}_{-0.15}$	–	–	1.36 (24)	1.39 (27)	$4.19^{+0.47}_{-0.47}$	$3.52^{+0.47}_{-0.47}$
Ch1	$0.60^{+0.05}_{-0.05}$	$2.00^{+0.12}_{-0.12}$	$1.86^{+0.12}_{-0.11}$	–	–	0.72 (34)	0.74 (35)	$5.38^{+0.32}_{-0.31}$	$4.93^{+0.32}_{-0.31}$
XM3	$0.40^{+0.06}_{-0.05}$	$2.20^{+0.15}_{-0.15}$	$2.39^{+0.17}_{-0.16}$	–	–	0.79 (27)	0.91 (30)	$2.38^{+0.25}_{-0.26}$	$3.07^{+0.25}_{-0.26}$
XM4	$0.65^{+0.09}_{-0.07}$	$2.21^{+0.18}_{-0.17}$	$1.99^{+0.17}_{-0.16}$	–	–	0.92 (73)	0.92 (76)	$5.20^{+0.62}_{-0.63}$	$4.17^{+0.62}_{-0.63}$
XM5	$0.61^{+0.07}_{-0.06}$	$2.04^{+0.12}_{-0.11}$	$1.93^{+0.11}_{-0.11}$	–	–	1.62 (47)	1.55 (50)	$3.53^{+0.30}_{-0.30}$	$3.32^{+0.30}_{-0.30}$
XM6	$0.36^{+0.04}_{-0.04}$	$2.22^{+0.16}_{-0.15}$	$2.56^{+0.19}_{-0.18}$	–	–	0.71 (57)	0.84 (60)	$1.87^{+0.19}_{-0.19}$	$2.73^{+0.19}_{-0.19}$
XM7	$0.53^{+0.02}_{-0.02}$	$2.15^{+0.05}_{-0.05}$	$2.13^{+0.05}_{-0.05}$	–	–	1.27 (229)	1.27 (232)	$3.92^{+0.14}_{-0.14}$	$3.90^{+0.14}_{-0.14}$
				tbabs × discbb					
XM1	$0.16^{+0.04}_{-0.03}$	–	–	$1.12^{+0.12}_{-0.10}$	$1.00^{+0.14}_{-0.11}$	1.81 (35)	1.78 (38)	$0.97^{+0.09}_{-0.09}$	$1.01^{+0.09}_{-0.09}$
XM2	$0.22^{+0.07}_{-0.05}$	–	–	$1.16^{+0.14}_{-0.12}$	$1.15^{+0.15}_{-0.13}$	1.52 (24)	1.53 (27)	$2.02^{+0.23}_{-0.23}$	$1.80^{+0.23}_{-0.23}$
Ch1	$0.32^{+0.05}_{-0.04}$	–	–	$1.34^{+0.11}_{-0.10}$	$1.50^{+0.18}_{-0.15}$	0.70 (34)	0.79 (35)	$3.14^{+0.18}_{-0.18}$	$3.04^{+0.18}_{-0.18}$
XM3	$0.10^{+0.06}_{-0.05}$	–	–	$1.18^{+0.13}_{-0.11}$	$1.03^{+0.14}_{-0.12}$	0.94 (27)	1.18 (30)	$1.22^{+0.13}_{-0.13}$	$1.42^{+0.13}_{-0.13}$
XM4	$0.33^{+0.08}_{-0.06}$	–	–	$1.16^{+0.15}_{-0.13}$	$1.32^{+0.22}_{-0.18}$	0.91 (73)	0.92 (76)	$2.64^{+0.31}_{-0.32}$	$2.39^{+0.31}_{-0.32}$
XM5	$0.29^{+0.06}_{-0.05}$	–	–	$1.33^{+0.12}_{-0.10}$	$1.42^{+0.15}_{-0.13}$	1.26 (47)	1.22 (50)	$2.04^{+0.17}_{-0.17}$	$2.02^{+0.17}_{-0.17}$
XM6	$0.13^{+0.04}_{-0.03}$	–	–	$1.09^{+0.12}_{-0.10}$	$0.94^{+0.14}_{-0.12}$	0.78 (57)	0.92 (60)	$0.98^{+0.10}_{-0.10}$	$1.13^{+0.10}_{-0.10}$
XM7	$0.25^{+0.02}_{-0.02}$	–	–	$1.29^{+0.05}_{-0.04}$	$1.33^{+0.05}_{-0.05}$	1.02 (229)	1.03 (232)	$2.24^{+0.08}_{-0.08}$	$2.23^{+0.08}_{-0.08}$
				tbabs × (po+discbb)					
XM7**	$0.25^{+0.02}_{-0.02}$	$0.87^{+0.37}_{-0.22}$	–	$1.21^{+0.01}_{-0.01}$	–	1.02 (228)	–	$2.23^{+0.01}_{-0.01}$	–

Notes. *These values were calculated using a fixed $N_{\rm H}$ value as 0.51×10^{22} cm^{-2} for the pl and 0.22×10^{22} cm^{-2} for the discbb models.
**Normalization parameters are 1.76×10^{-6} photon keV^{-1} cm^{-2} s^{-1} at 1 keV for the pl model and 6.58×10^{-3} $[(r_{\rm in}\ {\rm km}^{-1})/(D/10\ {\rm kpc})]^2 \times \cos i$ for the discbb model.
[a]Photon index of the pl component.
[b]Inner disc temperature.
[c]Reduced χ^2_ν.
[d]Unabsorbed luminosity values were calculated using a distance of 7.7 Mpc in the 0.3–10 keV energy range.

net count rate of the source is 0.06 count s^{-1} within the periods of flaring, while it is 0.04 count s^{-1} outside flaring episodes.

The *Chandra* data reduction was performed with the Interactive Analysis of Observations (CIAO) software (v4.9). The level-2 event files were obtained using the *chandra_repro* script in CIAO. The source X-3 was located on the ACIS-S3 (back-illuminated) chip. The source and background photons were extracted with the *specextract* task using 5-arcsec circular regions.

The *NuSTAR* data, on the other hand, were analysed using the *nupipeline* tool based on the *NuSTAR* Data Analysis Software (NUSTARDAS, v1.7.1) within the HEASOFT software and calibration data CALDB version 20191219. The source and background photons were extracted using 30-arcsec circular regions. In *NuSTAR* data reduction, the background regions were extracted from source-free regions close to X-3. Prior to fitting, the spectrum was grouped to have a minimum of 35 counts per bin.

The X-ray spectral fits were applied to the source spectra to interpret the origin of the X-ray emission and also to search for any spectral transitional behaviour. *XMM–Newton* and *Chandra* spectral fits were performed using the XSPEC package (v12.9.1) in the 0.3–10 keV energy band. All spectra were grouped to have a minimum of 20 counts per bin before the fitting procedure. *XMM–Newton* EPIC PN and MOS data were fitted simultaneously by adding a constant model for instrumental calibration differences. The best-fitting spectra were then obtained from the power-law (pl) and disc blackbody (discbb) models, together with two absorption models (tbabs). One of the absorption models represented the line-of-sight column density, which we kept fixed at the Galactic value ($N_{\rm H} = 0.01 \times 10^{22}$ cm^{-2}: Dickey & Lockman 1990), and the other was left free to account for intrinsic absorption. The unabsorbed flux values were calculated using the CFLUX convolution model in the 0.3–10 keV energy band. The luminosity values were obtained by considering the adopted distance of NGC 4258 (7.7 Mpc). The best-fitting model parameters for all observations are given in Table 2. The energy spectra for XM7 and C1 data are given in Fig. 2. To investigate whether flux variability occurred during the observations, the fitting process was repeated by fixing the intrinsic $N_{\rm H}$ parameters to the average of the calculated values in the initial fitting. The model parameters calculated with this method are also given in Table 2, denoted by '$*$', and we note that the flux variability between *XMM–Newton* observations is less than a factor of two.

The long-term light curve of the source was constructed using the available X-ray data (Table 1) to examine the flux variability. We used flux values obtained from the pl model in the range 3–10 keV. No significant variability was visible and the source exhibits a factor of 2.8 difference between the lowest and highest flux values. The long-term light curve of X-3 is given in Fig. 3.

Spectral fitting was also carried out especially for *XMM–Newton+NuSTAR* spectra, to investigate whether the cut-off is seen with *NuSTAR* or if there is perhaps an extra component in the high-energy spectrum (Bachetti et al. 2013; Pintore et al. 2017; West et al. 2018; Brightman et al. 2018).

We derived the best fitting single-component model parameters for X-3, given in Table 3. Two-component spectral fitting was also per-

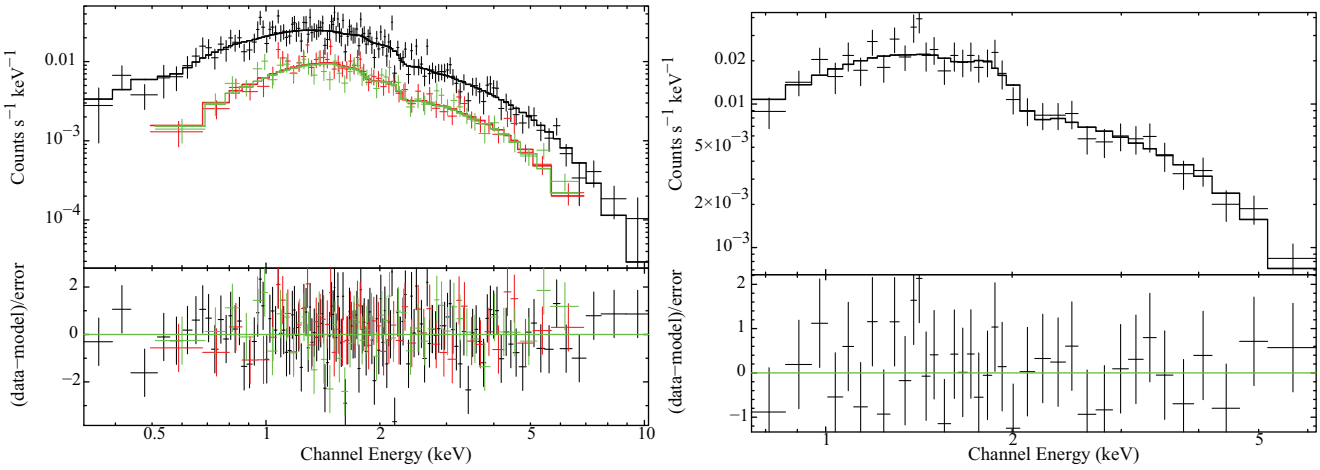

Figure 2. Energy spectra of X-3 obtained using XM7 (left) and C1 (right) data. In the *XMM–Newton* spectrum, the black, green, and red data points represent EPIC PN, MOS1, and MOS2, respectively. The *XMM–Newton* and *Chandra* spectra were fitted with the discbb model. Residuals of the fitting process are shown in the bottom panels.

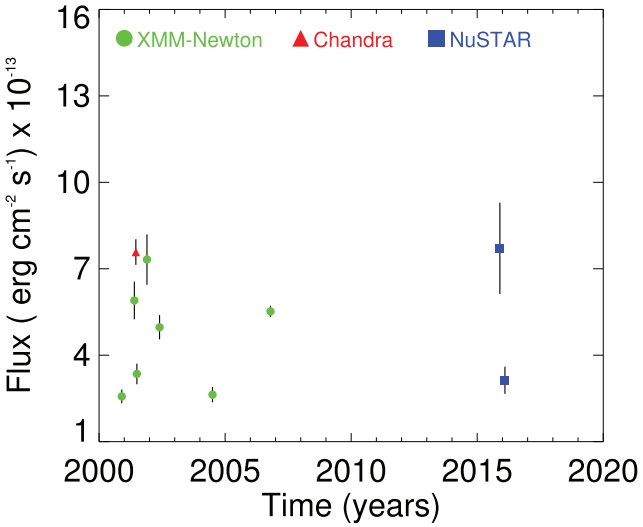

Figure 3. Long-term light curve of X-3 obtained using all X-ray data. Circles (green), triangles (red), and squares (blue) represent *XMM–Newton*, *Chandra*, and *NuSTAR* data, respectively. The fluxes were calculated in the 3–10 keV energy range.

formed with long-exposure data of *NuSTAR* (N2) and *XMM–Newton* (XM7) in the energy range 0.3–30 keV. The best-fitting parameters for the two-component model are given in Table 4. Although the dates of the two data sets are 9 years apart, fitting was performed based on the fact that the source does not show significant variability. A similar fitting process was applied by using $N_{\rm H}$ parameters as described above. The spectra obtained are given in Fig. 4.

In order to search for an underlying pulsar (neutron star), *XMM–Newton* EPIC PN data were used to perform timing analyses. The X-ray light curves of X-3 were sampled at 0.1 s and the resultant power-density spectra (PDS) were calculated. In addition, X-ray light curves were detrended using a second-degree polynomial to clean the excessive red noise at lower frequencies in the PDS. The PDS were calculated from a single interval, or up to 12 spectra were averaged to produce a PDS in the 0.3–10 keV band. We have searched for significant peaks in the PDS given a continuum red noise level. Significance levels were determined by fitting the power spectra with a two-component model of a Lorentzian and a constant. The significance is calculated as $\sigma = (P_{\rm max} - P_{\rm con})/P_{\rm err}$, where $P_{\rm max}$ is the power of the selected peak in the PDS, $P_{\rm con}$ is the continuum value around the peak, and $P_{\rm err}$ is the error in the peak value of power (Balman 2010). We did not find any peak with a significance large than 1.4σ for all PDS we analysed. Thus, we cannot confirm any

Table 3. Spectral parameters obtained with one-component model fits for X-3 with *XMM–Newton*+*NuSTAR* (N2).

Model	$N_{\rm H}$ (10^{22}) cm^{-2}	Γ	$kT_{\rm in}$ /$kT_{\rm e}$ [a] keV	$E_{\rm cut}$ [b] keV	p[c]	τ[d]	χ^2/dof	$L_{\rm X}$ (10^{39}) erg s^{-1}
pl	$0.58^{+0.02}_{-0.02}$	$2.27^{+0.04}_{-0.03}$	–	–	–	–	300.18/232 (1.29)	4.67
discbb	$0.25^{+0.02}_{-0.01}$	–	$1.31^{+0.01}_{-0.01}$	–	–	–	260.10/232 (1.12)	2.29
discpbb	$0.37^{+0.02}_{-0.02}$	–	$1.60^{+0.01}_{-0.01}$	–	$0.58^{+0.004}_{-0.003}$	–	251.75/231 (1.09)	2.78
compTT	$0.57^{+0.02}_{-0.02}$		$53.44^{+0.88}_{-0.89}$	–	–	$0.34^{+0.01}_{-0.01}$	296.58/230 (1.29)	3.77
cutoffpl	$0.33^{+0.02}_{-0.02}$	$0.84^{+0.04}_{-0.03}$	–	$2.49^{+0.08}_{-0.08}$	–	–	248.26/231 (1.07)	2.62

Notes. [a]Electron temperature of the corona.
[b]The e-folding energy of the cutoffpl model.
[c]Exponent of the radial dependence of the disc temperature.
[d]Optical depth of the corona.

Table 4. Spectral parameters obtained with two-component model fits for X-3 with *XMM–Newton* (XM7)+*NuSTAR* (N2).

Parameter	Unit	discbb+compTT	discbb+cutoffpl	discpbb+compTT	discpbb+cutoffpl
$N_{\rm H}$	10^{22} cm^{-2}	$0.31^{+0.02}_{-0.02}$	$0.28^{+0.02}_{-0.02}$	$0.29^{+0.02}_{-0.02}$	$0.28^{+0.02}_{-0.02}$
$kT_{\rm in}$	keV	$1.15^{+0.01}_{-0.01}$	$1.12^{+0.01}_{-0.01}$	$1.15^{+0.01}_{-0.01}$	$1.12^{+0.01}_{-0.01}$
p		–	–	$0.75^{+0.01}_{-0.01}$	$0.75^{+0.01}_{-0.01}$
N^a	10^{-3}	$6.93^{+0.32}_{-0.32}$	$8.09^{+0.34}_{-0.33}$	$60.7^{+3.20}_{-3.22}$	$8.37^{+0.35}_{-0.35}$
$kT_{\rm e}$	keV	$45.00^{+3.45}_{-3.46}$	–	50	
τ		$1.17^{+0.19}_{-0.16}$	–	$0.95^{+0.31}_{-0.22}$	–
Γ		–	$0.98^{+0.11}_{-0.09}$	–	$1.04^{+0.11}_{-0.09}$
$E_{\rm cut}$	keV	–	$15.39^{+7.92}_{-4.56}$	–	$16.14^{+8.80}_{-4.88}$
N^b	10^{-6}	$2.05^{+0.29}_{-0.29}$	$6.11^{+1.15}_{-1.12}$	$0.8^{+0.1}_{-0.1}$	$6.87^{+1.25}_{-1.21}$
χ^2/dof		1.04 (236.39/228)	1.03 (235.72/229)	1.03 (236.29/228)	1.03 (235.76/228)
Null P		0.34	0.45	0.39	0.27
$L_{\rm X}$ [c]	10^{39} erg s^{-1}	$1.69^{+0.01}_{-0.02}$	$2.58^{+0.01}_{-0.01}$	$2.33^{+0.01}_{-0.01}$	$2.78^{+0.01}_{-0.02}$

Notes. [a]Normalization parameters of discbb and discpbb models. $N = [(r_{\rm in}\ {\rm km}^{-1})/(D/10\ {\rm kpc})]^2 \times \cos i$.
[b]Normalization parameters of compTT and cutoffpl model in units of photon keV^{-1} cm^{-2} s^{-1} at 1 keV.
[c]Luminosity values were calculated for the 0.3–30 keV energy range.

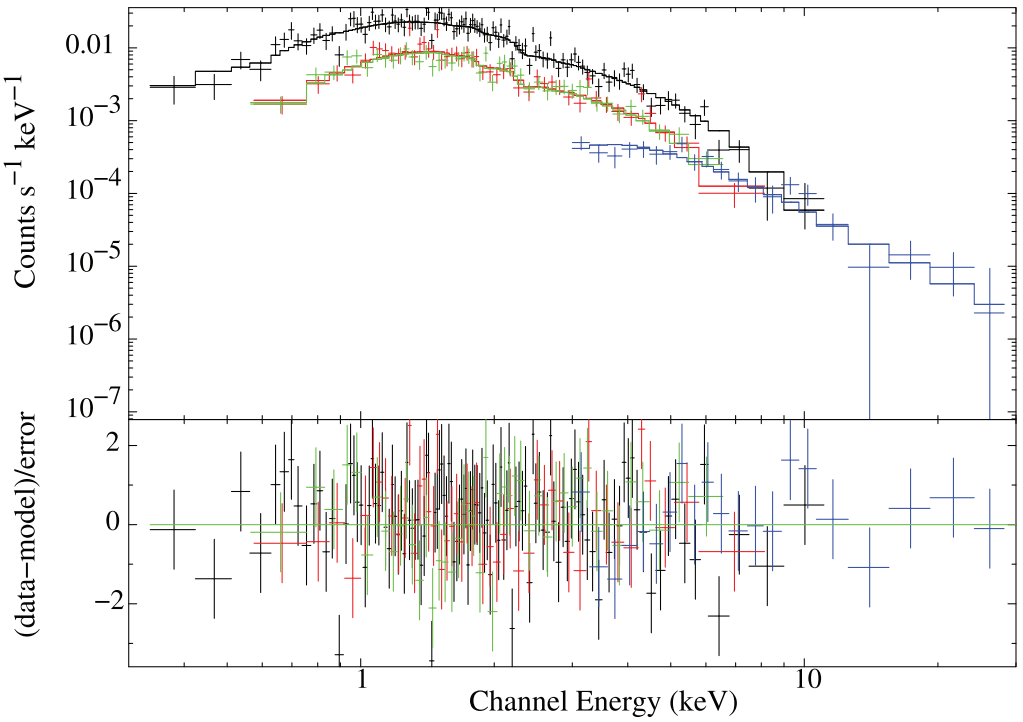

Figure 4. *XMM–Newton* + *NuSTAR* fitted spectra of X-3 in the 0.3–30 keV range. Black, red, green, and blue crosses are EPIC PN, MOS1, MOS2, and *NuSTAR* (FPMA+FPMB) data, respectively. The spectrum was fitted with the discbb+compTT model. The residual to the discbb+compTT model is shown in the bottom panel.

periodicity at $\geq 3\sigma$ confidence level. We note that our time-bin size of 0.1 s sets a lower limit for periods that were searched.

2.2 Astrometry and *HST* observations

Identification of the optical candidates for X-3 in NGC 4258 requires accurate source positions. An intercomparison of *Chandra*, *HST*, and Sloan Digital Sky Survey (SDSS) observations was carried out to obtain improved astrometry. We chose a deep *Chandra* The Advanced CCD Imaging Spectrometer (ACIS) observation (ObsID 1618) and an *HST* observation with the Advanced Camera for Surveys (ACS; ObsID JB1F89010). An SDSS (Alam et al. 2015) *r*-band image was also chosen. The CIAO tool *wavdetect* was used to detect discrete sources in ACIS-S. We selected four close, unique, isolated, and bright sources in both *Chandra* and SDSS images to be confident in the astrometry. These sources seem to be a group, but they are not spatially located in specific parts of the CCD. In this case, the vignetting effect is not considered. The matched pairs of objects in the comparisons are presented in Table 5. The positional uncertainties are given at 90 per cent confidence level for the *Chandra*/SDSS reference sources. The astrometric errors for *Chandra*−SDSS are RA 0.″02, Dec. 0.″15, and those for SDSS−*HST* comparisons are RA 0.″63, Dec. 0.″04. The final corrections used to translate the *Chandra* position of X-3 on to the *HST* image are

Table 5. Coordinates and their uncertainties for the X-ray/optical reference sources and ULXs.

Chandra RA	*Chandra* Dec.	SDSS RA	SDSS Dec.	Position uncertainty (arcsec)[a]	Counts[b]
Chandra ACIS X-ray sources (ObsID 1618) identified in SDSS observation (band *r*)					
12:18:49.488	+47:16:46.56	12:18:49.478	+47:16:46.47	0.166	140
12:18:59.335	+47:18:20.59	12:18:59.388	+47:18:20.45	0.807	11
12:18:56.165	+47:18:58.43	12:18:56.119	+47:18:58.14	0.736	13
12:18:57.506	+47:18:14.47	12:18:57.504	+47:18:14.38	0.095	2900
SDSS sources (*r* band) identified in *HST* ACS/WFC/F555W observation of JB1F89010					
SDSS RA	SDSS Dec.	*HST* RA	*HST* Dec.		
12:18:55.032	+47:15:53.57	12:18:55.075	+47:15:53.63	0.651	–
12:18:57.528	+47:15:30.28	12:18:57.578	+47:15:30.46	0.741	–
12:18:55.838	+47:15:34.23	12:18:55.874	+47:15:34.34	0.551	–
12:18:54.110	+47:15:37.83	12:18:54.149	+47:15:37.92	0.579	–
12:18:53.750	+47:15:57.80	12:18:53.806	+47:15:57.77	0.828	–
12:18:54.751	+47:14:43.04	12:18:54.806	+47:14:43.19	0.841	–
12:18:56.244	+47:14:51.12	12:18:56.268	+47:14:50.85	0.454	–
12:18:52.056	+47:16:53.13	12:18:52.094	+47:16:53.18	0.578	–
Corrected X-3 coordinates on SDSS and *HST* image					
SDSS RA	SDSS Dec.	*HST* RA	*HST* Dec.		
12:18:57.859	+47:16:07.44	12:18:57.902	+47:16:07.62		

Notes.[a]The uncertainties are given at the 90 per cent confidence level of the *Chandra*/*SDSS* reference sources.
[b]The background-subtracted counts were calculated in the 0.3–10 keV range using XSPEC.

Table 6. The log of *HST*/ACS observations.

Filter	ObsID	Date	Exp. (ks)
ACS/F606W	j96h39020	2005-03-13	1.01
ACS/F435W	jb1f98q8q	2009-12-03	0.36
ACS/F555W	jb1f98010	2009-12-03	0.98
ACS/F814W	jb1f98q5q	2009-12-03	0.38
ACS/F435W	jb1f89eoq	2009-12-14	0.36
ACS/F555W	jb1f89010	2009-12-14	0.98
ACS/F814W	jb1f89elq	2009-12-14	0.38

$0\overset{''}{.}65 \pm 0\overset{''}{.}33$ in RA and $0\overset{''}{.}18 \pm 0\overset{''}{.}09$ in Dec. These comparisons give uncertainties that are a quadratic sum of the standard deviations. Then the corrected position of X-3 is determined as RA $= 12^{h}18^{m}57\overset{s}{.}90$, Dec. $= +47^{\circ}16'07\overset{''}{.}62$ within the 90 per cent confidence level of an error circle with 0.28 arcsec radius. A similar calculation was also used by Wang et al. (2015).

We have analysed archival *HST* images obtained with ACS, given in Table 6. Point Spread Function (PSF) photometry was performed using the ACS module in DOLPHOT (v2.0, Dolphin 2000). The images were processed by masking all bad pixels using the *acsmask* task and the multi-extension ∗.fits files were split into single-chip images using the *Splitgroups* task before performing photometry. Then the sky background for each chip was calculated with the *calcsky* task. We ran the *dolphot* task on both bias and flat-field corrected ∗.flt and ∗.drz images. This task was used for photometry on the images by taking the F555W drizzled image as the positional reference in both epochs. Magnitudes in the VEGAmag and Johnson systems for the possible optical counterparts are given in Table 7.

After the astrometric correction and photometry, we checked the position of X-3 to find its optical candidates. Two optical candidates were identified within the error radius of 0.28 arcsec. The corrected position of X-3 on the *HST*/ACS images is shown in Fig. 5, together with the optical candidates. These candidates are labelled C1 and C2, according to decreasing Dec. coordinates.

The Galactic extinction along the direction of NGC 4258 is $E(B-V) \approx 0.014$ mag (Schlafly & Finkbeiner 2011). However, there are two extragalactic extinction studies in the literature. The first study from Kudritzki et al. (2013) derived $E(B-V) = 0.23 \pm 0.03$ using a blue supergiant star in the disc of NGC 4258, 48 arcsec south-east of X-3 (37.8 pc / 1 arcsec). The second study from Macri et al. (2006) gave 281 Cepheid stars with $E(B-V)$ values in the range 0.01–0.44 in NGC 4258. Following the second study, we obtained the extragalactic extinction $E(B-V) \approx 0.17$ by selecting about 30 Cepheids close to the X-3 region (≈160 arcsec north-west). The standard deviation of the extinction from the Cepheids is calculated as 0.08 mag. These two extragalactic extinction values (0.17 and 0.23) were used to determine the spectral type of the optical candidates. Both values yielded compatible results. Therefore, the average value $E(B-V) = 0.20$ was adopted as the extinction value throughout this work. The extinction-corrected magnitudes and colour values of the optical candidates are given in Table 7. The average standard deviation (0.08) does not affect the features of the counterparts significantly.

In order to estimate the age and mass of the optical candidates, colour–magnitude diagrams (CMDs) of X-3 and its environment were obtained. Two CMDs, for F555W versus F435W−F555W and F814W versus F555W−F814W, were derived for the optical candidates and the field stars. These stars are within the 25-arcsec^2 square region around X-3 shown in Fig. 1. The metallicity of NGC 4258 was chosen as $Z = 0.011$ from Kudritzki et al. (2013) to obtain the corresponding PARSEC isochrones. In Figs 6 and 7, the age and mass isochrones have been overplotted on the CMDs. The distance modulus was calculated as 29.4 mag using the adopted distance of 7.7 Mpc.

The spectral types of C1 and C2 were estimated using spectral energy distribution (SED) templates with PYSYNPHOT[1] using the CK04 standard stellar spectra (Castelli & Kurucz 2004). The SEDs for C1 and C2 are constructed for all flux values, which are derived from *HST*/ACS magnitudes in Table 7. Synthetic spectra

[1]https://pysynphot.readthedocs.io/en/latest/

Table 7. The dereddened magnitude and colour values of optical candidates of X-3 obtained from *HST*/ACS data. The F435W, F555W, and F814W filters correspond to *B*, *V*, *I* in the Johnson *BVI* system, respectively.

Date	Filter	VEGAmag		Johnson mag	
		1	2	1	2
2005-03-13	F606W	23.22 ± 0.02	23.26 ± 0.02	–	–
	F435W	23.09 ± 0.04	22.97 ± 0.03	23.13 ± 0.04	23.02 ± 0.03
2009-12-03	F555W	23.07 ± 0.03	23.03 ± 0.03	23.02 ± 0.03	23.00 ± 0.03
	F814W	22.74 ± 0.03	23.16 ± 0.04	22.73 ± 0.03	23.15 ± 0.04
	$(B-V)_0$			0.11	0.02
	M_V			−6.41	−6.43
	F435W	23.15 ± 0.04	22.90 ± 0.03	23.17 ± 0.04	22.96 ± 0.03
2009-12-14	F555W	23.06 ± 0.03	23.11 ± 0.03	23.01 ± 0.03	23.09 ± 0.03
	F814W	22.71 ± 0.03	23.31 ± 0.04	22.70 ± 0.03	23.30 ± 0.04
	$(B-V)_0$			0.16	−0.13
	M_V			−6.42	−6.34

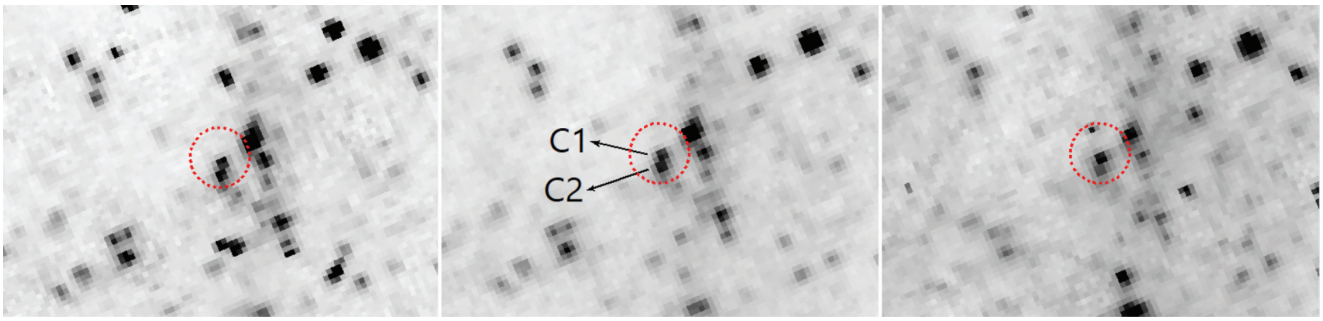

Figure 5. The *HST*/ACS images of X-3 in three filters: F814W, F555W, and F435W (from left to right). The dashed red circles represent the corrected position of X-3 with an accuracy of 0.28 arcsec error radius. Two optical candidates (C1 and C2) are shown within the error circle on the F555W image. There is a cosmic ray within the error circle on the F814W image.

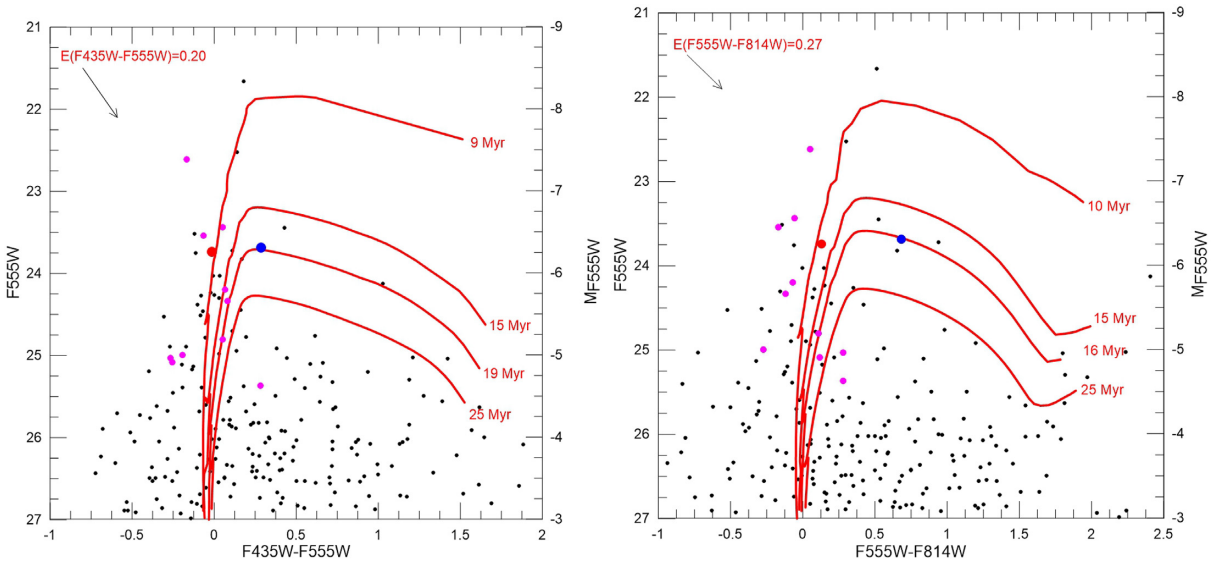

Figure 6. The *HST*/ACS colour−magnitude diagrams (CMDs) for optical candidates and field stars around X-3. Padova isochrones of different ages are overplotted. The blue and red dots represent optical candidates C1 and C2, respectively. The black and magenta dots represent field stars within the 25-arcsec^2 square region around X-3 and nearby stars, respectively. These isochrones have been corrected for extinction of $A_V = 0.62$ mag and the black arrows show the reddening line.

are normalized to $m_V = 0$ mag. The reduced χ^2 values of the best fits are 3.93 and 2.26, respectively. The resultant SEDs of C1 and C2 were found using the best-fitting models given in Fig. 8.

3 DISCUSSION AND CONCLUSIONS

In this study, archival X-ray data of X-3 in the nearby galaxy NGC 4258 were analysed. There are 10 X-ray observations of the source obtained by *XMM–Newton*, *Chandra*, and *NuSTAR* observatories

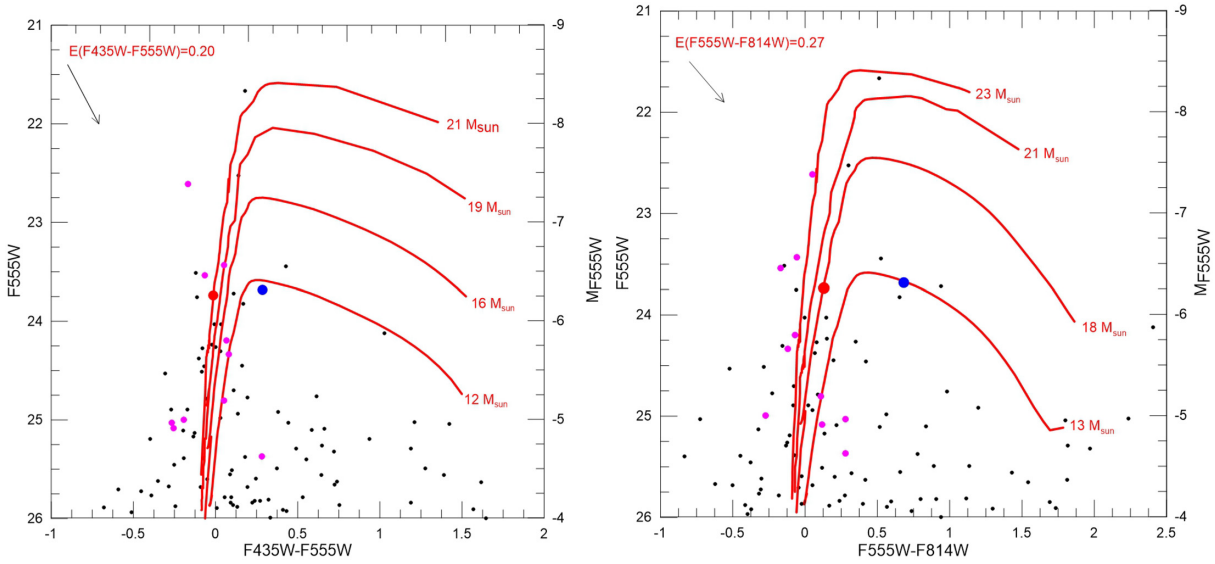

Figure 7. The *HST*/ACS CMDs for optical candidates and field stars around X-3. Padova isochrones of different masses are overplotted. Definitions are the same as in Fig. 6.

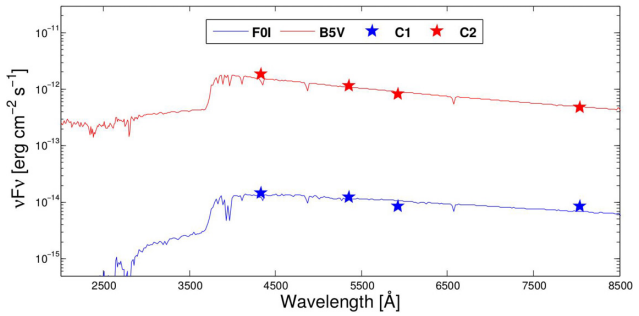

Figure 8. The SEDs of optical candidates C1 and C2. The blue and red lines represent the synthetic spectra derived with metallicity $Z = 0.011$ and extinction $A_V = 0.62$ mag for F0I and B5V, respectively. The blue and red circles represent flux values of candidates for C1 and C2, respectively. There is a systematic error of less than 3 per cent. The red line was shifted upward by a factor of 100 for clarity.

covering ≈15 years. The optical properties of the source were also studied with the *HST* observations. Two optical candidates were found within an 0.28-arcsec error radius and they were examined further.

In spectral analyses of the *XMM–Newton* and *Chandra* data, the spectral fits obtained show a wide range of χ^2_ν values going from 0.7 (which means that the data could be undersampled) to 1.8 (which means that the fit is not a good one). If we consider the application of simple phenomenological models for the obtained spectra of the source, we note that the discbb model fits better than the pl model at a 3σ confidence level for the XM5 and XM7 datasets (according to an *F*-test). On the other hand, the spectra of XM1 and XM2 fit the pl model better at $2–3\sigma$. However, it is not possible to distinguish between these two models for the remaining datasets: XM3, XM4, XM6, and Ch1.

Using the results from Gladstone et al. (2009), we elaborate on some of the spectral characteristics of X-3. The spectra of XM1 and XM2 are better represented by the pl model with photon index $\Gamma \sim (2–2.2)$. These Γ values correspond to hard states defined for Galactic BHBs. A hard state with low luminosity is seen at sub-Eddington mass accretion rates. On the other hand, the discbb model yields acceptable fits for XM5 and XM7 within a temperature range $kT_{\rm in} \sim (1.09–1.33)$ keV. These $kT_{\rm in}$ values are compatible with those of Galactic BHBs at high mass accretion rate during the thermal state (Remillard & McClintock 2006). Generally, in Galactic BHBs, luminosities are usually higher in the thermal state than in the hard state. However, we might interpret that X-3 exhibits the opposite behaviour, since the source has a high $L_{\rm X}$ when it is in a hard state and a low $L_{\rm X}$ when it is in a thermal state. There are some ULXs that do show similar behaviour: NGC 1313 X-2, Feng & Kaaret (2006); IC 342 X-1, Marlowe et al. (2014); NGC 4736 X-2, Avdan et al. (2014). As discussed in several studies, when the data quality is low and exposure is short, one-component models should be taken into account statistically. However, these models do not provide physically sufficient evidence to interpret the data (Gladstone et al. 2009; Sutton et al. 2013; Kaaret et al. 2017). Therefore, we combined two continuum models (pl and discbb) and fitted all data sets accordingly to examine the spectral characteristics and classification according to the prescription of Sutton et al. (2013). In their work, an empirical scheme is used to classify ULXs into three classes due to their spectral morphology: broadened disc, two-component hard ultraluminous, and two-component soft ultraluminous classes. When we applied the two-component model to available data, we were only able to obtain physically meaningful parameters for XM7. The spectrum of XM7 is adequately fitted with the doubly absorbed (discbb + pl) spectral model ($\Gamma = 0.87$ and $kT_{\rm in} \sim 1.21$ keV) with $\chi^2_\nu \sim 1.01$ as given in Table 2. Due to the very flat photon index Γ, it is fixed to values between 1.7 and 2 (no acceptable fit outside this range); however, $kT_{\rm in}$ and χ^2_ν values were not changed significantly. The best-fitting temperature parameter ($kT_{\rm in} = 1.21$ keV) is $>$ 0.5 keV, based on the chart in the form of a decision tree in fig. 2 of Sutton et al. (2013), while the calculated $F_{\rm pl}/F_{\rm disc}$ ratio is found to be 0.29 (Γ was fixed at 1.7 while calculating $F_{\rm pl}$), which indicates that the X-3 spectrum can be classified as a 'broadened disc'. Sutton et al. (2013) defined that the broadened disc class ULX population has $L_{\rm X} < 3 \times 10^{39}$ erg s^{-1} and this is consistent with a population of stellar-mass black holes ($M < 20\ {\rm M}_\odot$) accreting at just above the Eddington limit. The spectra of this class are thought to be dominated by the

accretion disc but, due to the high accretion rate, the disc structure is modified from the standard thin disc.

Pulsating ULXs (PULXs) are known to show luminosity variabilities of at least a factor of 100 (Fürst et al. 2016; Israel et al. 2017a, b; Rodríguez Castillo et al. 2020). However, the source X-3 exhibits a variability usually less than a factor of 3 throughout observations spanning 15 years. This may be another clue pointing to a black hole as the compact accretor rather than a neutron star. Then, by using the discbb model's normalization parameter $N = (R_{\rm in} / D_{10})^2 \cos\theta$ (defined by Makishima et al. 2000), the mass of the compact object in the system can also be estimated. In the formula, $R_{\rm in}$ is the inner disc radius in km, D_{10} is the distance to the source in units of 10 kpc, and θ is the inclination angle of the disc. We calculated the mass using the best-fitting normalization parameter of the discbb model ($N_{\rm disc} = 5.5 \pm 0.2 \times 10^{-3}$) derived for the longest exposure data, XM7. The inner disc radius was found to be $R_{\rm in} = 95$ km (using the equation $R_{\rm in} = \xi\kappa^2 r_{\rm in}$, where the correction factor $\xi = 0.41$, spectral hardening factor $\kappa = 1.7$, and $r_{\rm in}$ is the apparent inner disc radius; see Shimura & Takahara 1995; Kubota et al. 1998). Assuming a moderate disc inclination of 60°, we can calculate the mass of the compact object as $\sim$10 $M_\odot$, indicating a stellar-mass black hole.

We also used data from *NuSTAR* observations (which have an energy range of 3–79 keV) for further understanding of the X-3 system. Although the *NuSTAR* observations are not simultaneous with the *XMM–Newton* ones in time, due to low variability of the X-3 system, joint analysis of both data is performed to examine the emission of the source at high energies (>10 keV). The spectral results using one-component model fits are summarized in Table 3. The models provide slightly better fits for a discpbb or a cutoffpl model with luminosity $L_{\rm x} \sim 2.7 \times 10^{39}$ erg s^{-1}. We also investigated whether the spectral fits are improved over one-component model fits by adding a second component in modelling. We found that derived $E_{\rm cut}$ values for one- and two-component models are in accordance with the findings in the literature (Rana et al. 2015; Krivonos & Sazonov 2016; Shidatsu, Ueda & Fabrika 2017; Koliopanos et al. 2019). The results are given in Table 4. This joint analysis was constructed to test the differences in spectral characteristics of ULXs and PULXs, as in the study by West et al. (2018). The discbb/discpbb model was used, along with either a compTT model for a black hole interpretation, where a seed-in temperature from the disc is connected with the Comptonized plasma in/above the disc, or a cutoffpl model for a neutron-star accretor interpretation, where the emission is from the accretion column. The temperature parameter of compTT is fixed to 50 keV while applying the discpbb+compTT model to the spectra. This temperature is similar to that seen in Galactic BHBs while they are in classical accretion states (Gladstone et al. 2009; Bachetti et al. 2013). The p parameters were found to be consistent with the standard disc model ($p \sim 0.75$). In this case, models containing the disc model (with one or two components) may be more favourable. Nevertheless, these models did not yield any distinguishable fits considering reduced χ^2 values and null-hypothesis probabilities. In addition, F-test probability values ($\sim 10^{-5}$) did not show any significant improvement of the fits over the one-component models. As a result, *NuSTAR* data jointly analysed with *XMM–Newton* data did not help us to elaborate further on our ULX model for X-3, which predicts a black hole as a compact accretor.

Using the usual CMD techniques, the derived mean age values of the optical candidates C1 and C2 are $\approx$18 and $\approx$10 Myr, respectively, as described in Section 2.2. Assuming the optical emission is dominated by the donor star, the spectral types of the possible optical counterparts are found to be A3−F1 giant for C1 and B3−B6 main-sequence star for C2. Similarly, the SEDs from stellar templates (CK04) of C1 and C2 candidates match with spectral types F0I and B5V, respectively. Their masses can also be constrained using mass isochrones $\approx$13 $M_\odot$ and 20 $M_\odot$ for C1 and C2, respectively. Both optical candidates of X-3 are young blue stars with $(B-V)_0$ values in the range −0.13–0.16.

There is a distinct arm in the region of X-3 where new star formation seems quite dense, as seen from Fig 1. We also investigate the environment of X-3 within a 25-arcsec^2 region. Although there was no obvious star cluster near the ULX source, the selected 12 stars with magenta colour represent the bright stars very close to X-3 shown in Figs 6 and 7. These bright stars in the CMD have ages < 40 Myr and their $(B-V)$ colours are between −0.4 and 0.4, with $m_{\rm V} \approx$ 22.5–25.5 mag. The ages and colour values of the candidates of X-3 and the stars in the selected region seem compatible with each other.

In order to differentiate the optical candidates from background AGNs, we obtained their X-ray to optical flux ratios. We used XM7 and *HST*/ACS F555W (ObsID JB1F89010) data sets for these calculations, since simultaneous observations are not available for these wavelengths. $F_{\rm X}/F_{\rm opt}$ values for C1 and C2 were found to be 390 and 360, respectively. On the other hand, ratios for active galactic nuclei are in the range $0.1 \leq (F_{\rm X}/F_{\rm opt})_{\rm AGN} \leq 10$ (Aird et al. 2010). These ratio values of optical candidates of X-3 are significantly higher than those of AGNs, but are compatible with known ULXs: $260 < F_{\rm X}/F_{\rm opt} < 4200$ (Avdan et al. 2016a, b).

We believe observers of the ULX source X-3 in NGC 4258 will make use of broadband X-ray spectra obtained at higher sensitivity and observation sampling to study the source spectra and their possible spectral variations. Further joint longer observations using *XMM–Newton* and *NuSTAR* may allow us to constrain the characteristics of the X-ray emission components and perform better timing analyses. Ongoing missions like *eROSITA*/SRG and future missions like *Athena* can resolve the complexities we have outlined in our work.

ACKNOWLEDGEMENTS

We thank the anonymous referee for providing very helpful comments. We also thank M.E. Özel for his valuable contributions and suggestions. This research was supported by the Scientific and Technological Research Council of Turkey (TÜBİTAK) through project number 117F115. This research was also supported by the Çukurova University Research Fund through project number FBA-2019-11803.

DATA AVAILABILITY

The scientific results reported in this article are based on archival observations made by the *Chandra X-ray Observatory*[2], as well as archival observations by *XMM–Newton*[3], an ESA science mission with instruments and contributions directly funded by ESA Member States and NASA, and archival observations by the *NuSTAR*[4] mission, a project led by the California Institute of Technology, managed by JPL and funded by NASA. This work has also made use of observations made with the NASA/ESA *Hubble Space Telescope*[5]

[2]https://cda.harvard.edu/chaser/
[3]http://nxsa.esac.esa.int/nxsa-web/#search
[4]https://heasarc.gsfc.nasa.gov/docs/nustar/nustar_archive.html
[5]https://archive.stsci.edu/hst/search.php

and obtained from the data archive at the Space Telescope Science Institute. STScI is operated by the Association of Universities for Research in Astronomy, Inc. under NASA contract NAS 5-26555.

REFERENCES

Abolmasov P. K., Swartz D. A., Fabrika S., Ghosh K. K., Sholukhova O., Tennant A. F., 2007, ApJ, 668, 124
Aird J. et al., 2010, MNRAS, 401, 2531
Aksaker N., Akyuz A., Avdan S., Avdan H., 2019, MNRAS, 488, 5935
Alam S. et al., 2015, ApJS, 219, 12
Avdan H., Kayaci Avdan S., Akyuz A., Balman S., 2014, Ap&SS, 352, 123
Avdan S. et al., 2016a, MNRAS, 455, L91
Avdan H., Avdan S., Akyuz A., Balman S., Aksaker N., Akkaya Oralhan I., 2016b, ApJ, 828, 105
Avdan S. et al., 2019, ApJ, 875, 68
Bachetti M. et al., 2013, ApJ, 778, 163
Bachetti M. et al., 2014, Nature, 514, 202
Balman Ş., 2010, MNRAS, 407, 1895
Brightman M. et al., 2018, ApJ, 867, 110
Carpano S., Haberl F., Maitra C., Vasilopoulos G., 2018, MNRAS, 476, L45
Castelli F., Kurucz R. L., 2004, A&A, 419, 725
de Vaucouleurs G., de Vaucouleurs A., Corwin, Herold G. J., Buta R. J., Paturel G., Fouque P., 1991, Third Reference Catalogue of Bright Galaxies. Springer, New York
Dickey J. M., Lockman F. J., 1990, ARA&A, 28, 215
Dolphin A. E., 2000, PASP, 112, 1383
Fabrika S., Ueda Y., Vinokurov A., Sholukhova O., Shidatsu M., 2015, Nature Physics, 11, 551
Farrell S. A., Webb N. A., Barret D., Godet O., Rodrigues J. M., 2009, Nature, 460, 73
Feng H., Kaaret P., 2006, ApJ, 650, L75
Fürst F. et al., 2016, ApJ, 831, L14
Fürst F., Walton D. J., Stern D., Bachetti M., Barret D., Brightman M., Harrison F. A., Rana V., 2017, ApJ, 834, 77
Gladstone J. C., Roberts T. P., Done C., 2009, MNRAS, 397, 1836
Gladstone J. C., Copperwheat C., Heinke C. O., Roberts T. P., Cartwright T. F., Levan A. J., Goad M. R., 2013, ApJS, 206, 14
Grisé F., Kaaret P., Pakull M. W., Motch C., 2011, ApJ, 734, 23
Grisé F., Kaaret P., Corbel S., Feng H., Cseh D., Tao L., 2012, ApJ, 745, 123
Heida M. et al., 2014, MNRAS, 442, 1054
Heida M., Jonker P. G., Torres M. A. P., Roberts T. P., Walton D. J., Moon D. S., Stern D., Harrison F. A., 2016, MNRAS, 459, 771
Israel G. L. et al., 2017a, Science, 355, 817
Israel G. L. et al., 2017b, MNRAS, 466, L48
Jonker P. G. et al., 2012, ApJ, 758, 28
Kaaret P., Feng H., Roberts T. P., 2017, ARA&A, 55, 303
King A., Lasota J.-P., 2016, MNRAS, 458, L10
Koliopanos F., Vasilopoulos G., Buchner J., Maitra C., Haberl F., 2019, A&A, 621, A118
Krivonos R., Sazonov S., 2016, MNRAS, 463, 756
Kubota A., Tanaka Y., Makishima K., Ueda Y., Dotani T., Inoue H., Yamaoka K., 1998, PASJ, 50, 667
Kudritzki R.-P., Urbaneja M. A., Gazak Z., Macri L., Hosek, Matthew W. J., Bresolin F., Przybilla N., 2013, ApJ, 779, L20
López K. M., Heida M., Jonker P. G., Torres M. A. P., Roberts T. P., Walton D. J., Moon D.-S., Harrison F. A., 2017, MNRAS, 469, 671
Luangtip W., Roberts T. P., Done C., 2016, MNRAS, 460, 4417
Macri L. M., Stanek K. Z., Bersier D., Greenhill L. J., Reid M. J., 2006, ApJ, 652, 1133
Makishima K. et al., 2000, ApJ, 535, 632
Marlowe H. et al., 2014, MNRAS, 444, 642
Mezcua M., Roberts T. P., Lobanov A. P., Sutton A. D., 2015, MNRAS, 448, 1893
Miller M. C., Colbert E. J. M., 2004, Int. J. Mod. Phys. D, 13, 1
Motch C., Pakull M. W., Soria R., Grisé F., Pietrzyński G., 2014, Nature, 514, 198
Pakull M. W., Mirioni L., 2003, Rev. Mex. Astron. Astrofís. Conf. Ser., 15, 197
Patruno A., Zampieri L., 2010, MNRAS, 403, L69
Pintore F., Zampieri L., Stella L., Wolter A., Mereghetti S., Israel G. L., 2017, ApJ, 836, 113
Poutanen J., Fabrika S., Valeev A. F., Sholukhova O., Greiner J., 2013, MNRAS, 432, 506
Rana V. et al., 2015, ApJ, 799, 121
Remillard R. A., McClintock J. E., 2006, ARA&A, 44, 49
Roberts T. P., 2007, Ap&SS, 311, 203
Rodríguez Castillo G. A. et al., 2020 , ApJ, 895, 60
Sathyaprakash R. et al., 2019, MNRAS, 488, L35
Schlafly E. F., Finkbeiner D. P., 2011, ApJ, 737, 103
Shidatsu M., Ueda Y., Fabrika S., 2017, ApJ, 839, 46
Shimura T., Takahara F., 1995, ApJ, 445, 780
Soria R., Cropper M., Pakull M., Mushotzky R., Wu K., 2005, MNRAS, 356, 12
Stobbart A. M., Roberts T. P., Wilms J., 2006, MNRAS, 368, 397
Sutton A. D., Roberts T. P., Middleton M. J., 2013, MNRAS, 435, 1758
Swartz D. A., Soria R., Tennant A. F., Yukita M., 2011, ApJ, 741, 49
Tao L., Feng H., Grisé F., Kaaret P., 2011, ApJ, 737, 81
Vinokurov A., Fabrika S., Atapin K., 2018, ApJ, 854, 176
Wang S., Liu J., Bai Y., Guo J., 2015, ApJ, 812, L34
West L. A. et al., 2018, ApJ, 869, 111
Wiktorowicz G., Sobolewska M., Lasota J., Belczynski K., 2017, ApJ, 846, 17

This paper has been typeset from a TEX/LATEX file prepared by the author.